Tungsten Bronze Barium Neodymium Titanate ($Ba_{6-3n}Nd_{8+2n}Ti_{18}O_{54}$): an Intrinsic Nanostructured Material and its Defect Distribution

Feridoon Azough[†], Robert Joseph Cernik[†], Bernhard Schaffer[‡§], Despoina-Maria Kepaptsoglou[†‡], Quentin Mathieu Ramasse[‡], Marco Bigatti[§], Amir Ali[§], Ian MacLaren[§], Juri Barthel[+], Marco Molinari[$], Jakub Dominik Baran[$], Stephen Charles Parker[$] and Robert Freer[†,*]

[†]School of Materials, University of Manchester, M13 9PL, UK

[‡]SuperSTEM, SciTech Daresbury, Keckwick Lane, Warrington WA4 4AD, UK

[§]SUPA School of Physics and Astronomy, University of Glasgow, Glasgow G12 8QQ, UK

+Central Facility for Electron Microscopy, RWTH Aachen University, Ahornstr. 55, 52064 Aachen, Germany

[$]Department of Chemistry, University of Bath, Claverton Down, Bath, BA2 7AY, UK

[*]**corresponding author:** Robert.Freer@manchester.ac.uk

Abstract

We investigated the structure of the tungsten bronze barium neodymium titanates, $Ba_{6-3n}Nd_{8+2n}Ti_{18}O_{54}$, which are exploited as microwave dielectric ceramics. They form a complex nanostructure, which resembles a nanofilm with stacking layers of approximately 12Å thickness. The synthesized samples of $Ba_{6-3n}Nd_{8+2n}Ti_{18}O_{54}$ (n = 0, 0.3, 0.4, 0.5) are characterized by pentagonal and tetragonal columns where the A cation are distributed in 3 symmetrically inequivalent sites. Synchrotron X-ray diffraction and Electron Energy Loss Spectroscopy allowed for quantitative analysis of the site occupancy, which determines the defect distribution. This is corroborated by Density Functional Theory calculations. Pentagonal columns are dominated by Ba and tetragonal columns by Nd respectively, although specific Nd sites exhibit significant concentrations of Ba. The data indicated significant elongation of the Ba columns in the pentagonal positions and of the Nd columns in tetragonal positions involving a zig-zag arrangement of atoms along the b lattice direction. We found that the preferred Ba substitution occurs at Nd[3]/[4] followed by Nd[2] and Nd[1]/[5] sites, which is significantly different to that proposed in earlier studies. Our results on the $Ba_{6-3n}Nd_{8+2n}Ti_{18}O_{54}$ 'perovskite' superstructure and its defect distribution are particularly valuable in those applications where the optimization of material properties of oxides is imperative; these include not only microwave ceramics but also thermoelectric materials, where the nanostructure and the distribution of the dopants will reduce the thermal conductivity.

Keywords: Microwave ceramic, Titanate, Thermoelectric oxide, Nanostructured oxide, EELS, DFT

I. Introduction

Microwave dielectric ceramics, having high relative permittivity (ε_r), low dielectric loss (described by tan δ, or $Q = 1/\tan \delta$) and tuneable temperature coefficient of resonant frequency (τ_f) are important components in a wide range of terrestrial and satellite communications systems[1-5]. Whilst the relative permittivities of such dielectrics range from 20 to 110, the family of tungsten-bronze-structure ceramics based on $Ba_{6-3n}Ln_{8+2n}Ti_{18}O_{54}$ (Ln=La, Nd, Pr, Sm) display the highest relative permittivity materials, with ε_r values typically in the range of 80 to 110. They are also characterised by low dielectric loss, giving them Qxf values (where f is frequency) which can exceed 10,000 GHz, and near-zero τ_f[2,3,6-8].

There has long been debate over the true stoichiometry of the compounds. The earliest work on $BaO\text{-}Nd_2O_3\text{-}TiO_2$ dielectrics is attributed to Bolton[9], but Kolar *et al.*[10,11], investigating TiO_2-rich compositions of the $BaO\text{-}Nd_2O_3\text{-}TiO_2$ ternary system, are credited with the identification of important high-dielectric-constant, low-dielectric-loss, low-temperature-coefficient-of-capacitance compounds equivalent to $BaNd_2Ti_5O_{14}$ and $BaNd_2Ti_3O_{10}$ (giving 1:1:5 and 1:1:3 ratios for the ternary components). Razgon *et al.*[12,13] reported the existence of the intermediate (1:1:4) compound $BaLn_2Ti_4O_{12}$ (Ln=La, Gd), which was later confirmed by Takahashi *et al.*[14,15] for $BaLn_2Ti_4O_{12}$ (Ln=La, Nd, Sm). Jaakola *et al.*[16] proposed that the true stoichiometry is closer to $Ba_{3.75}Nd_{9.5}Ti_{18}O_{54}$, whilst Valant and co-workers[17,18] reported the occurrence of single phase $BaGd_2Ti_4O_{12}$. These discrepancies in the reported compositions were explained by Varfolomeev *et al.*[19], who showed that all the compositions belong to a solid solution with the general formula $Ba_{6-3n}Nd_{8+2n}Ti_{18}O_{54}$. This was later confirmed by Ohsato *et al.*[20], who demonstrated that the solid solution exists over the composition range $0.0<n<0.7$, whilst for n values greater than 0.8 a second phase, $Nd_4Ti_9O_{24}$, was formed.

There have also been many investigations to establish the space group and crystal structure for this solid solution, predominantly using X-ray diffraction. Matveeva *et al.*[21] reported that $Ba_{3.75}Pr_{9.5}Ti_{18}O_{54}$ (n=0.75) crystallized in an orthorhombic system. Although the presence of a superstructure doubling the c-axis was found, they refined structural parameters by assuming an average cell with a non-centrosymmetric space group *Pba2*. Using electron diffraction techniques, Azough *et al.*[22] determined the space group of $BaPr_2Ti_4O_{12}$ compound to be *Pnma*. Subsequently, Rawn[23] undertook powder X-ray diffraction studies of the Gd and La analogues with n=0.5, employing space groups of *Pnma* and $Pna2_1$ respectively for the refinement of the two materials. Rawn *et al.*[24] also investigated by X-ray diffraction the structure of single crystals of the Sm analogue, $Ba_{6-3n}Sm_{8+2n}Ti_{18}O_{54}$, for n=0.27. Superstructure reflections, which cause a doubling of the cell along the short axis, were taken into account and the refinement was conducted in the orthorhombic space group *Pnma*. The unit cell parameters were determined to be a=22.289(1)Å,

b=7.642(1)Å, and c=12.133(1)Å. The perovskite-like structure (of these solid solution materials) is made up of a network of corner-sharing TiO_6 octahedra creating tetragonal and pentagonal channels. The pentagonal channels are fully occupied by Ba atoms. The refinement suggested that there are 3 types of tetragonal channels: one fully occupied by Sm atoms (Sm[3]/[4]), one partially occupied by Sm atoms (100% Sm[1] / 86.25% Sm[5]), and one shared by Ba/Sm atoms (59.25% Ba[3] / 40.75% Sm[2]), resulting in a formula of $Ba_{10.38}Sm_{17.08}Ti_{36}O_{108}$. Later Okudera *et al.*[25] reported the existence of a solid solution for the Sm analogue over the composition range $0.3<n<0.7$ and refined the structural parameters in the centrosymmetric space group *Pbam*, with the unit cell characterized by five crystallographically-independent sites in the tetragonal tunnels and two sites in pentagonal tunnels. Sm was expected to be located in the perovskite-like tetragonal tunnels while the larger Ba ions were in the pentagonal tunnels. To maintain charge neutrality in compositions with different Ba/Nd ratios, the presence of vacancies was suggested and a scheme for Ba, Sm and vacancy distribution was proposed:

$$(Sm_{8+2n}\,Ba_{2-3n}\,\square_n)\,[Ba_4]\,Ti_{18}O_{54}\ (n < 2/3),\ (Sm_{8+2n}\,\square_n)\,[Ba_{6-3n}\,\square_{3n-2}]\,Ti_{18}O_{54}\ (n \geq 2/3) \qquad (1)$$

where parentheses and squares brackets designate tetragonal and pentagonal sites respectively, and open squares designate vacancies.

In our latest study[26], we investigated the structure of ceramic $Ba_{4.5}Nd_9Ti_{18}O_{54}$ by synchrotron X-ray powder diffraction from 10 to 295K. Rietveld refinement and Le Bail profile analysis were applied to the data, which resulted in a satisfactory refinement using the space group *Pnma*, with unit cell parameters of a=22.3479(3)Å, b=7.6955(1)Å, and c=12.2021(2)Å at room temperature and a=22.3367(5)Å, b=7.6738(1)Å, and c=12.1842(3)Å at 10K. No evidence was found for any structural change from 10 to 295K. Within the tungsten-bronze framework the two pentagonal channels were fully occupied by Ba; the remaining Ba atoms were assumed to share the tetragonal channels with Nd. There are two crystallographically-independent pentagonal sites [designated A1(1) and A2(1)] and five perovskite-like sites [A2(1) to A2(5)]. Nd is located in the perovskite-like layers (five A2 sites) and depending on the Ba/Nd ratio Ba will occupy the A1 sites and possibly the A2 sites; at lower ratios Ba occupies the pentagonal A1 sites, whilst at higher Ba/Nd ratios the excess Ba enters the tetragonal A2 sites. Figure 1 shows schematic [010] projection of the $Ba_{6-3n}Nd_{8+2n}Ti_{18}O_{54}$ Tungsten Bronze Barium structure according to Tang *et al.*[26]. There are 5 different Nd lattice sites where certain positions overlap in [010] projection, namely Nd[1] and Nd[5] henceforth assigned as column type **1**, Nd[3] and Nd[4] as column type **3**, and Nd[2] as column type **2**.

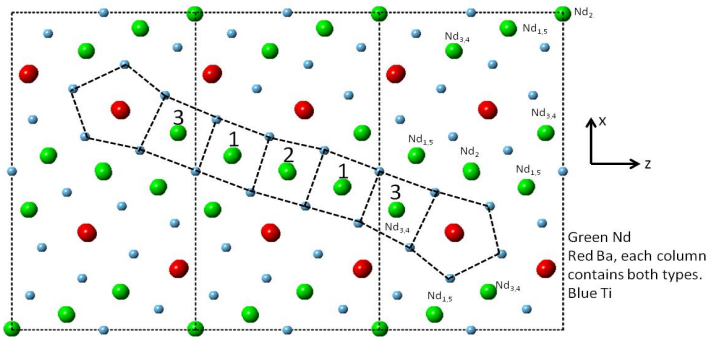

Figure 1. *[010] projection of the structure of $Ba_{4.5}Nd_9Ti_{18}O_{54}$ showing pentagonal channels and three types of tetragonal channels. The X and Z directions correspond to the a and c lattice parameters. Only the cation (Ba, Nd and Ti) positions are shown for clarity whereas the O positions are omitted. The pentagonal and tetragonal channels are shown with dashed lines. Five different Nd lattice sites are shown, Nd[1] and Nd[5] are assigned as column type 1, Nd[3] and Nd[4] as column type 3, and Nd[2] as column type 2.*

Although the proposed structural models [24,25,26] for $Ba_{6-3n}Ln_{8+2n}Ti_{18}O_{54}$ (Ln= Sm and Nd) are similar, the predictions of the distribution of excess Ba in the tetragonal sites are contrasting. Indeed, for $Ba_{6-3n}Sm_{8+2n}Ti_{18}O_{54}$ (n=0.27) single crystals, Rawn *et al.*[24] suggested that Ba substitutes only in type 2 columns in agreement with Tang *et al.*[26] for $Ba_{6-3n}Nd_{8+2n}Ti_{18}O_{54}$ (n=0.5) polycrystalline ceramics, but in contrast with Okudera *et al.*[25], who suggested excess Ba in type 1 columns in $Ba_{6-3n}Sm_{8+2n}Ti_{18}O_{54}$ (n = 0.3, 0.5, 0.67, 0.71). None of the studies have predicted substitution of Ba in type 3 sites.

In the present study, we have therefore investigated the crystal structure and cation site occupancy for the $Ba_{6-3n}Nd_{8+2n}Ti_{18}O_{54}$ (n = 0.0, 0.3, 0.4, 0.5) system. This perovskite-like system, due to its intrinsic superstructure made of stacking layers of approximately 12Å thickness (c axis) and complex defect distribution, is indeed a commercially-attractive system, not only as a microwave dielectric but also for those applications where nanostructuring becomes a fundamental engineering process to enhance materials properties. Perovskite oxides are indeed the most promising thermoelectric materials, but due to high thermal conductivity, their use is still limited. Understanding the structure and the distribution of defects in $Ba_{6-3n}Nd_{8+2n}Ti_{18}O_{54}$ is therefore the first step to understand whether its attractive structural properties can be implemented in other perovskite materials. We have therefore used atomic-resolution imaging and electron energy loss spectroscopy (EELS) analysis in an aberration-corrected scanning transmission electron microscope (STEM), in combination with high resolution X-ray diffraction to revisit $Ba_{6-3n}Nd_{8+2n}Ti_{18}O_{54}$ structure and composition. Complementary Density Functional Theory (DFT) calculations were performed to support the experimental findings. The combination of these techniques can indeed provide atom-level insights into the detailed atomic chemistry of this system, providing a definitive determination of structural properties.

II. Experimental Methods

(1) Ceramic Preparation. Ceramic samples of $Ba_{6-3n}Nd_{8+2n}Ti_{18}O_{54}$ (n=0, 0.3, 0.4, 0.5) were prepared by the conventional mixed-oxide route. Starting materials were high-purity (>99.5%) powders of $BaCO_3$ (Solvay, 99.5%), Nd_2O_3 (AMR Limited, 99.9%) and TiO_2 (Tioxide, 99.9%). The Nd_2O_3 was dried at 900°C for 6hr prior to use. The powders were weighed in batches according to the required formulations and wet-milled for 24hr in a vibratory mill using yttria stabilized zirconia balls and propan-2-ol. The milling process is not expected to cause more than 0.1 wt% contamination, with any Zr present entering Ti sites, and not sites occupied by Ba or Nd. After drying, the mixed batches were calcined at 1150°C for 4hr. The calcined batches were wet-milled for a further 24hr. Powders were uniaxially compacted into pellets of 20mm diameter and 15mm thickness at a pressure of 50MPa prior to sintering at 1350-1400°C for 4hr in air. The cooling rates were 180°C/hr for all compositions while additional samples for the composition with n=0 were also prepared at slower cooling rates of 6°C/hr and 1°C/hr.

(2) Physical Properties and Microstructure. Product densities were determined by the Archimedes method. Diffraction data were collected on the I11 powder diffraction beamline at the Diamond light source. The sub-micron crushed powders of each composition were placed in a capillary tube and the data collected at ambient temperature in 2Θ range of 5-100 degrees. The data-collection wavelength was 0.826989Å. Rietveld analysis of the data was undertaken using TOPAS 4.2 software (Bruker AXS, Karlsruhe, Germany). Microstructures of as-sintered and polished surfaces were examined by scanning electron microscopy (Philips XL30 FEGSEM equipped with EDX capability). Samples were ground using SiC down to 1200 grade and polished using 6μm and 1μm diamond paste, followed by Oxide Polishing Suspension (OPS).

(3) Transmission Electron Microscopy. Samples for transmission electron microscopy were prepared by both ion-beam thinning and crushing techniques. For ion-beam thinning, the specimens were first ground on 1200 grade SiC to reduce the thickness to ~300μm. They were ultrasonically cut into 3mm diameter disks (Model KT150; Kerry Ultrasonic Ltd.) then dimpled (Model D500; VCR Group, San Francisco, CA) to reduce the thickness of the centre of the disk to 30μm. Finally, the disks were ion-beam thinned (using a Gatan Precision Ion Polishing System model 691; Gatan Inc., Pleasanton, CA) operating at 4–6kV. For the crushing method, the sintered disks were crushed to powder using an agate mortar and pestle. Grains of individual powders were dispersed in chloroform, dropped onto a copper grid with holey carbon film, and then dried. Structures were initially investigated using selected area electron diffraction (SAED) and high-resolution transmission electron microscopy (HRTEM) techniques using a FEI FEGTEM (Tecnai G2, Hillsboro, OR) operating at 300kV. Subsequently, STEM observation was performed at the SuperSTEM facility using the aberration-corrected Nion UltraSTEM100 (Nion Co., Kirkland, WA)

instrument equipped with a Gatan Enfina spectrometer (Gatan Inc., Pleasanton, CA). The microscope was operated at 100kV, with a probe convergence angle (α) of 30mrad. In these operating conditions the size of the electron probe is ~0.9Å. High-angle annular-dark-field (HAADF) imaging was performed using an annular detector with an inner semi-angle of 100mrad and an effective outer semi-angle of 185mrad. Electron energy loss spectra were collected using an acceptance angle (β) into the spectrometer entrance aperture of 31mrad. 2D EEL Spectrum Images were acquired by rastering the electron probe serially across a defined region and collecting an EEL spectrum at each point, using integration times of 0.05-0.1s/pixel and step widths of 0.05-0.08nm depending on the specific dataset to provide a good compromise between acquisition speed and spatial sampling. All EEL Spectrum Image acquisitions were single cycle and single read-out and full vertical binning (x100) of the spectrometer CCD was systematically used to maximize the signal-to-noise ratio. Chemical maps are created by integrating at each point of these spectrum images the spectrum intensity over an ~40 eV window above the Ba $M_{4,5}$, Nd $M_{4,5}$ and Ti $L_{2,3}$ ionisation edge onsets after background subtraction using a power law model.

(4) Statistical analysis of partitioning of Ba onto Nd sites. Statistical analysis was applied to evaluate the occupancies of Ba and Nd sites from atomic resolution electron energy loss spectrum images. Elemental maps were obtained by integrating the intensity under the Ba, Nd, and Ti ionisation edges at each pixel of the experimental spectrum images over a suitable energy window (chosen in particular to minimise any strong effect of the near-edge fine structure), after subtraction of the decaying background using a power-law model. The details of the background-fitting and signal-integration windows are given in Table 1 for reference. These maps can then be further processed and quantified to yield chemical compositions using the known values of the convergence and collections angles (α and β given above), together with the tabulated values for the inelastic cross-sections for the Ba $M_{4,5}$, Nd $M_{4,5}$ and Ti $L_{2,3}$ ionisation edges. It is well-known, however, that the calculations of inelastic cross-sections for M edges can be unreliable[27]. Additionally, electron channelling has a strong influence on intensities in atomic-resolution chemical mapping and the results from attempts at quantification are often not directly interpretable without the help of inelastic image simulations[28-30]. The large number of samples, compositions and parameters renders such calculations time-prohibitive. To overcome these difficulties, we therefore apply here the empirical approach based on an internal self-consistent normalisation procedure from the raw maps, adapted from Warusawithana *et al.*[31]

Table 1: *Background-extrapolation and signal-integration windows used for the calculation of elemental maps in Digital Micrograph software, together with cross-sections calculated using the standard Hartree-Slater method.*

Element and Edge	Background fit range (eV)	Signal fit range (eV)	Calculated cross section (barns)
Ba – $M_{4,5}$	697-765	781-821	3654 ± 365
Nd – $M_{4,5}$	873-958	978-1018	1261 ± 126
Ti – $L_{2,3}$	407-447	456-481	3269 ± 327

Each column in the Ba and Nd maps, and, where available, the Ti maps, was identified using a peak-finding algorithm and labelled according to its position in the unit cell (see atomic column position determination in section 5). The areal density counts were then integrated across a 3x3 box under each peak and the counts for each type of position are listed separately. A map of the n=0.4 sample was used as an internal reference: in this composition, the Ba content is relatively low and many seemingly Ba-free columns could be found in a number of experimental EELS maps. Note that the n=0.5 compound would have arguably been a more natural choice of internal reference given its even lower Ba content. In practice, however, fewer unequivocally Ba-free columns could be found in the acquired maps for this sample (due perhaps to the fact that the n=0.4 sample had lower thickness, thus yielded higher quality data: see further discussion of Figure 10). Nominally-pure Ba sites in this reference structure were used to estimate the uncorrected areal density of Ba expected around a pure Ba column. Similarly, a number of Nd[1] sites with the lowest detectable Ba intensity (therefore assumed to contain no Ba) were used to estimate the uncorrected areal density of Nd expected on a fully-occupied, nominally pure Nd column. All composition maps from the entire series of samples were then scaled using correction factors obtained by comparison to these reference maps, the Ba map values being for instance multiplied by a factor of 2.5216. Such reasonably large correction factors are not unexpected: with a closely-packed unit cell containing a number of heavy atomic columns, 'de-channelling' of electrons from Ba-containing columns onto neighbouring Nd-rich columns is very likely, thus making absolute values obtained from a direct quantification of the data highly unreliable. While full simulations of inelastic scattering in the sample would be necessary to accurately quantify the column occupancies from experimental maps, the internal normalisation procedure described has been shown to yield reliable results when applied to samples of known compositions[31]. It was used here as a convenient, albeit possibly approximate, way of estimating the relative column occupancies for further correlation with X-ray data and DFT calculations. For all sample compositions, an average and standard deviation of the Ba:Nd ratio in each independent Nd column was obtained by applying this procedure to experimental chemical maps recorded in [010] zone axis. In this projection, as illustrated in Figure 1, the Nd[1]-Nd[5] (henceforth denoted Nd[1]/[5] or column type **1**) and Nd[3]-Nd[4] (denoted as Nd[3]/[4] or column type **3**) columns overlapped, and thus we just report in Figure 1 (and later in

Figure 2) the contents for column types (by the number at the foot of the column) simply by **1**, **2** and **3**, corresponding to columns Nd[1]/[5], Nd[2] and Nd[3]/[4], respectively.

(5) Determination of atomic column positions. Series of over 20 consecutive HAADF images were recorded along the [010] zone-axis using very short dwell times of 5-10μs per pixel. Rigid registration of these image 'stacks' through cross-correlation and summation produces high signal-to-noise images[32], which allow the determination of atomic column coordinates with picometer precision[33-35]. Unless otherwise stated, all images shown in this manuscript were acquired in this fashion. The positions of the heavy-ion-containing A-site (Nd and Ba) columns were determined by 2D fitting of Gaussian profiles to each atomic column using the iMtools software[36] as used in previous quantitative atomic resolution electron microscopy studies[33-35,37]. The left edges of the images were systematically avoided due to possible scan distortions. A representative averaged unit cell was obtained from each image through template-matching, aligning by convention the c-axis (*z* coordinate) of the structure horizontally; when necessary, shear was corrected through the application of the appropriate 2x2 shear matrix to the individual cropped cells prior to averaging. A preliminary calibration of the unit cell sizes from pixels into Å was performed using the lattice parameters previously refined from X-ray data obtained in this study. As explained above, in the [010] projection, the Nd[1] and Nd[5] as well as Nd[3] and Nd[4] overlapped, so only the average positions for Nd[1]/[5], Nd[2] and Nd[3]/[4] can be reported here. The unit cells were then reduced to a list of symmetry-equivalent positions using the standard list of symmetry equivalent positions for the *Pnma* structure reduced to just the *x*-*z* plane of:

(a) x,z (b) $-x+½,z+½$ (c) $-x,-z$ (d) $x+½,-z+½$ (2)

This procedure yields mean atomic positions with uncertainties in *x* and *z* (a- and c-axes). Full three-dimensional unit cells were then generated using the *y* positions (b-axis) from the X-ray data of this study.

Frozen-phonon HAADF STEM image simulations were performed with the Dr. Probe software[38] using the atomic structure coordinates derived by the above method, with the purpose of evaluating the correspondence between the proposed structure models (after determination of the site chemical occupancies through analysis of the EELS data: see above) and experimental HAADF STEM images. The microscope parameters used in the image simulations were adjusted to resemble as closely as possible the experimental conditions, with primary beam energy of 100keV and with a 30mrad convergence angle of the electron probe. Coherent probe aberrations of C_3=5.7μm and C_5=−4.5mm were used, as measured, while other aberrations were set to zero for simplicity. The chromatic aberration was considered by applying an explicit focal averaging with a Gaussian focus-spread of 5nm 1/e half-width. An annular detection range between 100mrad and 185mrad was used. Primary images were calculated with 20 statistically independent frozen-phonon configurations per

scan pixel using the Einstein model of thermal motion. No object mistilt was considered for the elastic electron diffraction calculations. The calculated images were finally convoluted by a Gaussian of 1.1Å full-width at half-maximum (FWHM) to account for the geometrical source size (see below for an explanation of how this value was estimated) and other resolution limiting factors such as electrical and mechanical vibration as well as for imperfections of the image series averaging. Scan images were extracted for a thickness range up to 23nm (30 unit cells along the b axis) in steps of b/2=0.385nm.

An analysis of the average integrated image peak intensities of Nd and Ti columns over the simulated object thickness range shows a monotonously decreasing ratio falling from about 4.2 at 2nm thickness down to 1.5 at 23nm thickness in the case of the sample of composition n=0. This ratio was determined as the fraction of the integrated peak intensities under the Nd[1]/[5] column and the surrounding Ti positions. Similar ratios for the other types of Nd columns can be obtained for other compositions, and these exhibited similar behaviour. An integration radius of 0.13nm was used around each peak, which is below half-the-projected-distance of 0.29nm between the Nd and Ti columns. In the same way, intensity ratios were extracted from the experimental images after subtracting a global dark intensity value. Due to the monotony of the ratio over thickness observed in the simulations, the local thickness could therefore be estimated by simple comparison across the field-of-view for the various experimental images. This comparison thus allows a re-scaling of the intensities of experimental images, so both experimental and simulated images can be displayed for convenience on a similar scale, corresponding to a fraction of the incident beam current. (Note that this scale is not 'absolute' – a parameter-free, absolute comparison of experiment and simulation would require, among other parameters, a full characterisation of the detector response[38,39] prior to the acquisition instead of the simple, albeit informative, rescaling applied here). The whole analysis is so far largely independent of the effective source size, which was estimated in a final step by matching the peak maximum intensities of the rescaled experimental images and simulated images of the same thickness.

III. Computational Method

Spin polarized calculations were performed using the VASP[40,41] code. The core−valence interaction is represented using the PAW[42,43] approach. The valence electronic states are expanded in the basis of plane waves and the frozen core is [He] for O, [Ne] for Ti, [Kr] for Ba and [Xe] for Nd. The exchange-correlation functional applied was the PBE GGA with the inclusion of the Hubbard-U term using the Dudarev[44] approach. The GGA+U methodology[45] enables to account for the presence of the localized states and it is widely used for transition metals[46,47] and lanthanides[48]. U_{eff} values of 4eV and 5eV were chosen for the Ti d and Nd f orbitals. The cut-off energy for the plane

wave basis was 500eV with the Brillouin zone sampled using the Γ point. Constant pressure relaxation of the atomic structure was deemed to have converged when the forces were below $0.01 eVÅ^{-1}$. Convergence to the ground state was tested by imposing different starting magnetizations, and hence the configuration with the lowest total energy is selected for further study. The constraint was then removed and the system was allowed to relax. All systems relaxed to a ferromagnetic ordering with a spin-only magnetic moment on Nd^{3+} ions of $2.9\mu_B$. 3D boundary conditions were used throughout. All configurations were made by using the Metadise[49] code and all figures were drawn using the program VESTA[50]. Five configurations containing two unit-cells of stoichiometry $Ba_{6-3n}Nd_{8+2n}Ti_{18}O_{54}$ (n=0), for a total of 172 atoms and 1424 electrons, were simulated. The lattice parameters of the relaxed configurations are presented in Table 2 and Figure 2 shows a schematic representation of the configurations.

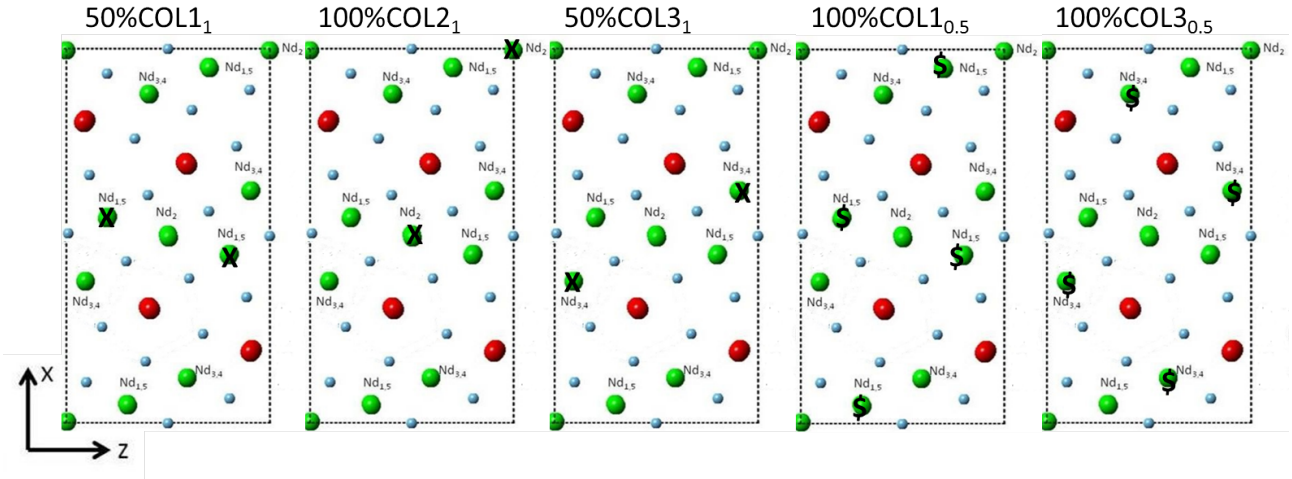

Figure 2. *[010] projection of the $Ba_{6-3n}Nd_{8+2n}Ti_{18}O_{54}$ (n=0). Five configurations were studied using DFT with different substitution of Ba in tetragonal columns. Nd[3]/[4], Nd[1]/[5] and Nd_2 represent Nd sites of tetragonal column 3, 1 and 2 respectively. X and $ signs represent 100% and 50% substitution of Ba on Nd sites. Green Nd, Red Ba and Blue Ti. X and Z directions represent the a and c lattice parameters.*

The structure contains pentagonal and tetragonal channels as shown in the [010] projection of the structure in Figure 1. Pentagonal columns are occupied by Ba ions while tetragonal columns are partially occupied by Nd/Ba ions. The structure has four columns type **1**, four columns type **3** and two columns type **2** per formula unit. To study the preferential Ba substitution on Nd sites, five configurations were made, namely 50%COL1$_1$, 100%COL2$_1$, 50%COL3$_1$, 100%COL1$_{0.5}$ and 100%COL3$_{0.5}$, by substituting four Ba ions on Nd sites. The acronym for the configurations is "% of columns with substitution" – "column number" – "fraction of substitution in each column". Thus, 50%COL1$_1$ and 50%COL3$_1$ have fully substituted sites in columns types 1 and 3 respectively but only 50% of the columns are substituted. 100%COL2$_1$ has 100% Ba substitution in columns type **2** and 100% of columns were fully substituted; this is because the unit cell only contains half-

the-number of columns type **2** compared to columns types **1** and **3**. Finally, 100%$COL1_{0.5}$ and 100%$COL3_{0.5}$ have Ba substitution in 100% of columns type **1** and **3** respectively but only 50% of substitution in each column; substitution was performed such that Ba ions were placed as far apart as possible to minimize Coulombic interactions.

Table 2. *DFT relaxed configurations of $Ba_{6-3n}Nd_{8+2n}Ti_{18}O_{54}$ (n=0) compared with the experimental lattice parameters of Tang et al.*[26]

Configuration	a (Å)	b (Å)	c (Å)	α (degree)	β (degree)	γ (degree)
50%$COL1_1$	23.0065	7.7432	12.5358	90.00	89.71	90.01
100%$COL2_1$	22.9603	7.7226	12.5479	90.00	90.01	90.00
50%$COL3_1$	23.2121	7.7347	12.5044	90.00	89.95	90.00
100%$COL1_{0.5}$	22.9994	7.7907	12.4676	90.00	90.00	90.00
100%$COL3_{0.5}$	23.5854	7.7364	12.4384	90.00	90.00	90.00
Tang et al. [26]	22.3479	7.6955	12.2021	90.00	90.00	90.00

IV. Results and Discussion

(1) Physical properties and Microstructure

We have undertaken the task of defining unambiguously the composition of the different columns in the $Ba_{6-3n}Nd_{8+2n}Ti_{18}O_{54}$ system. Thus high-purity samples were synthetized. All ceramics were of high density, exhibiting at least 95% of their theoretical density. The microstructures were characterised by needle-shaped grains. All products were single-phase except for the composition with n=0, which showed minor amounts of a secondary phase in the form of enlarged platelets (Figure 3). EDS analysis confirmed that the second phase is rich in Ba and Ti.

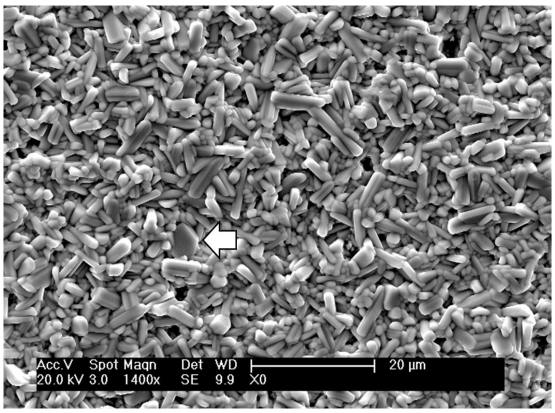

Figure 3. *SEM image for the n=0 sample showing the needle shape of the matrix grains and the second phase grain (arrowed).*

(2) Crystal structure determination from X-ray diffraction

X-ray diffraction data collected at station I11 of the Diamond Light Source was refined by the Topas software. Consistent with the SEM data, extra peaks with low intensity were observed in the X-ray diffraction spectrum for composition n=0. The extra peaks do not match any of the known Ba-Ti-O compounds. Zheng and West[51] observed a secondary phase for composition n=0 and identified it as cubic $BaTiO_3$ stabilized with small amount of Nd, whereas Ohsato *et al.*[20] reported an unknown phase for the Sm analogue. The change in the lattice parameters of $Ba_{6-3n}Nd_{8+2n}Ti_{18}O_{54}$ as function of n is shown in Figure 4a. The lattice parameters decrease as n increases, with the greatest change seen for the b-axis and the smallest for the c-axis. Due to this reduction for all three lattice parameters, the unit cell volume is reduced with increasing n (Figure 4b).

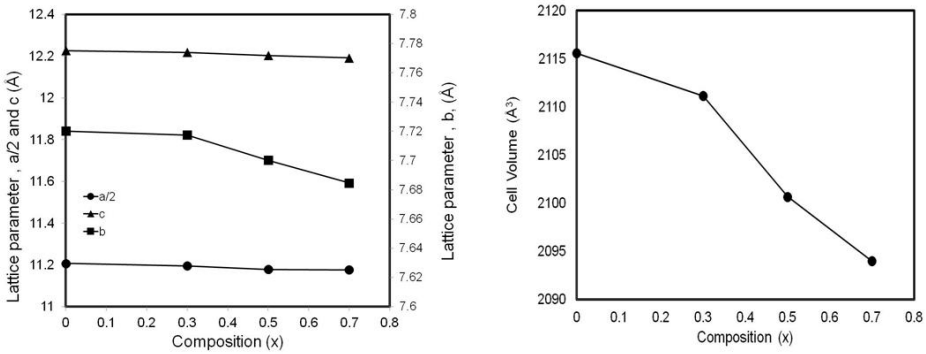

Figure 4. *a) Lattice parameters of $Ba_{6-3n}Nd_{8+2n}Ti_{18}O_{54}$ solid solution as a function of n obtained from I11data. The lattice parameters decrease in all three lattice direction with increasing n. b) Unit cell volume as a function of composition*

Figure 5 shows a Rietveld refinement of the crystal structure of one of the compositions (n = 0.3). The best refinement was obtained using space group Pnma[22]. It can be seen that there is a good fit (r_{wp} 7.07, GoF 1.12) between the observed and calculated data for 2161 reflections and 126 independent refinable parameters. However, we noticed that reflections of type (h 0 l) were broadened compared to reflections with other hkl values. From the SEM image of the microstructure (Figure 3) it is apparent that the grains exhibit a needle like habit, with average size of 2 x 2 x 15 microns; this is the case for all the compositions in this system. This grain size is too large to produce a significant particle size effect on the X-ray data but we believe that needle morphology is associated with larger stacking strain in the shorter crystal directions (which coincides with the a and c directions, the longer unit cell parameters). This leads to anisotropic strain which manifests itself in the broadening of (h 0 l) reflections. A Stephens correction[52] applied to all data sets significantly improves the fit in all cases. The Rietveld refined data for composition n = 0.3, after applying the Stephens correction, are shown in Figure 5. Refined positional, site

occupancy and isotropic thermal parameters for composition n=0.3 are summarized in Table 3. Site occupancies for all three compositions are presented in Table 4.

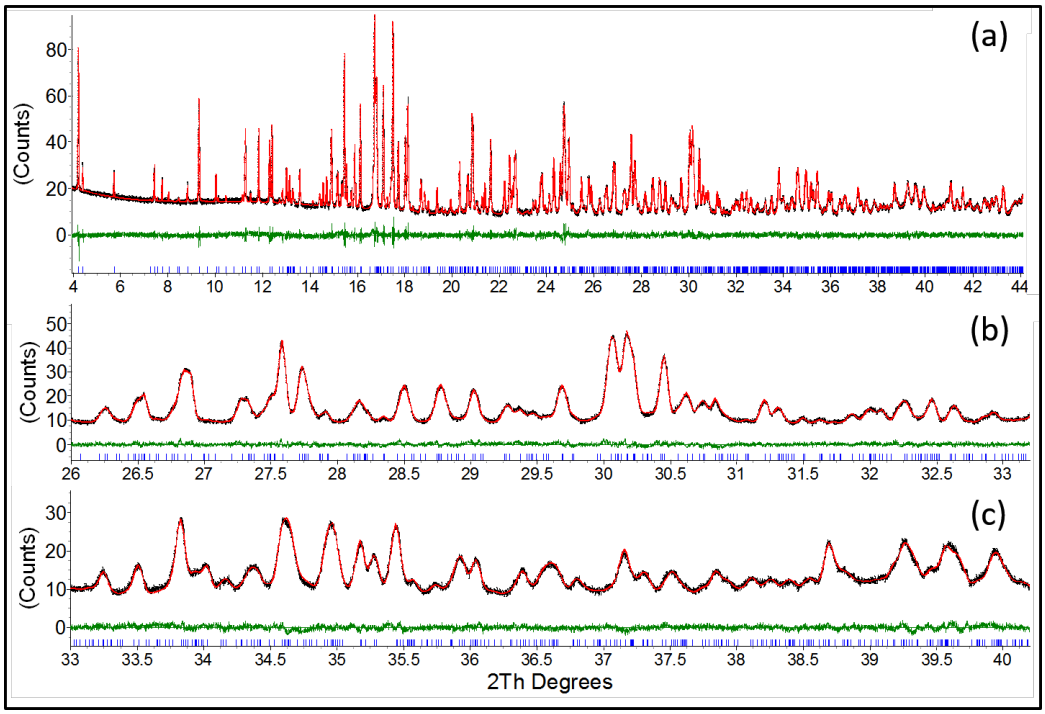

Figure 5. *The Rietveld refinement for composition n=0.3. The blue line is the experimental data, the red line is the calculated profile and the grey line represents the difference between them; (a) full spectrum, (b), and (c) are expanded regions, showing an excellent fit.*

Table 3. *Refined positional, occupancy, number of position in the unit cell (Np), and isotropic thermal parameters for composition n=0.3.*

Site	Np	x	y	z	Atom	Occupancy	Thermal parameter (B) ($Å^2$)
Ti1	4	0.50000	0.50000	0.00000	Ti^{+4}	1	0.596 (3)
Ti2	8	0.33496 (6)	0.5021 (5)	0.11635 (12)	Ti^{+4}	1	0.596 (3)
Ti3	8	0.39144 (6)	0.49987 (5)	0.39880 (13)	Ti^{+4}	1	0.596 (3)
Ti4	8	0.43506 (6)	0.4997 (6)	0.69853 (14)	Ti^{+4}	1	0.596 (3)
Ti5	8	0.26206 (7)	0.4991 (6)	0.83682 (12)	Ti^{+4}	1	0.596 (3)
Nd1	4	0.94840 (5)	0.25000	0.29508 (10)	Nd^{+3} Ba^{+2}	0.9 (2) 0.1 (3)	0.596 (3)
Nd2	4	0.49601 (6)	0.25000	0.50137 (15)	Nd^{+3} Ba^{+2}	0.76 (10) 0.21 (11)	0.596 (3)

Nd3	4	0.12241 (5)	0.25000	0.40820 (12)	Nd^{+3} Ba^{+2}	0.7 (2) 0.3 (2)	0.596 (3)
Nd4	4	0.37883 (5)	0.25000	0.90352 (12)	Nd^{+3} Ba^{+2}	0.7 (2) 0.3 (2)	0.596 (3)
Nd5	4	0.04709 (5)	0.25000	0.69715 (10)	Nd^{+3} Ba^{+2}	0.8 (3) 0.1 (3)	0.596 (3)
Ba6	4	0.80109 (4)	0.25000	0.91166 (11)	Ba^{+2}	1	0.596 (3)
Ba7	4	0.68682 (4)	0.25000	0.40390 (10)	Ba^{+2}	1	0.596 (3)
O1	8	0.4055 (2)	0.4659 (9)	0.5531 (3)	O^{-2}	1	0.596 (3)
O2	8	0.4780 (2)	0.5397 (9)	0.8455 (4)	O^{-2}	1	0.596 (3)
O3	8	0.4205 (2)	0.5404 (7)	0.0422 (4)	O^{-2}	1	0.596 (3)
O4	8	0.3617 (2)	0.5196 (11)	0.7643 (4)	O^{-2}	1	0.596 (3)
O5	8	0.3144 (2)	0.4825 (12)	-0.03345 (4)	O^{-2}	1	0.596 (3)
O6	8	0.38514 (19)	0.5210 (11)	0.24104 (4)	O^{-2}	1	0.596 (3)
O7	8	0.48159 (19)	0.5129 (13)	0.3722 (4)	O^{-2}	1	0.596 (3)
O8	8	0.1932 (2)	0.5026 (18)	-0.0826 (4)	O^{-2}	1	0.596 (3)
O9	8	0.2639 (2)	0.4894 (15)	0.1830 (3)	O^{-2}	1	0.596 (3)
O10	4	0.3318 (4)	0.75000	0.0969 (9)	O^{-2}	1	0.596 (3)
O11	4	0.4026 (4)	0.25000	0.3842 (7)	O^{-2}	1	0.596 (3)
O12	4	0.3552 (4)	0.25000	0.1052 (8)	O^{-2}	1	0.596 (3)
O13	4	0.5185 (4)	0.75000	0.0179 (8)	O^{-2}	1	0.596 (3)
O14	4	0.4466 (4)	0.25000	0.7268 (6)	O^{-2}	1	0.596 (3)
O15	4	0.2774 (5)	0.75000	0.8335 (9)	O^{-2}	1	0.596 (3)
O16	4	0.2750 (5)	0.25000	0.8225 (9)	O^{-2}	1	0.596 (3)
O17	4	0.4448 (4)	0.75000	0.6780 (6)	O^{-2}	1	0.596 (3)
O18	4	0.3964 (4)	0.75000	0.4181 (7)	O^{-2}	1	0.596 (3)

Table 4. *Site occupancies for the different compositions (cooled at 60°C/hour) obtained from I11X-ray diffraction data.*

Site	n=0.5	n=0.3	n=0.0
Nd[1]: Nd Nd[1]: Ba	0.84(13) 0.13(14)	0.9(2) 0.1(3)	0.8(4) 0.1(4)
Nd[2]: Nd	0.92(20)	0.76(10)	0.84(5)

Nd[2]: Ba	0.05(30)	0.21(11)	0.16(5)
Nd[3]: Nd Nd[3]: Ba	1.0(3) 0.0(3)	0.7(2) 0.3(2)	0.76(4) 0.30(5)
Nd[4]: Nd Nd[4]: Ba	1.0(3) 0.0(3)	0.7(2) 0.3(2)	0.8(3) 0.2(4)
Nd[5]: Nd Nd[5]: Ba	0.92(20) 0.05(30)	0.8(3) 0.1(3)	0.9(4) 0.1(4)

(3) STEM-EELS crystal structure and chemistry determination

The Z-contrast images shown in Figure 6a-b provide direct atomic evidence of the structural model depicted in Figure 1. Careful analysis reveals that the HAADF image contains three distinct intensity levels: bright columns correspond to Ba and Nd (or mixed columns) while lower intensity columns correspond to Ti. The dark positions are the vacant sites of the Tungsten Bronze structure. The HAADF image consists of V-shaped rows containing 7 atomic columns in each row. The pentagonal tunnels are at the end of each row and 5 tetragonal tunnels are in-between pentagonal tunnels; similar images were recorded for all compositions and all cooling rates and the structures of all samples were visibly similar.

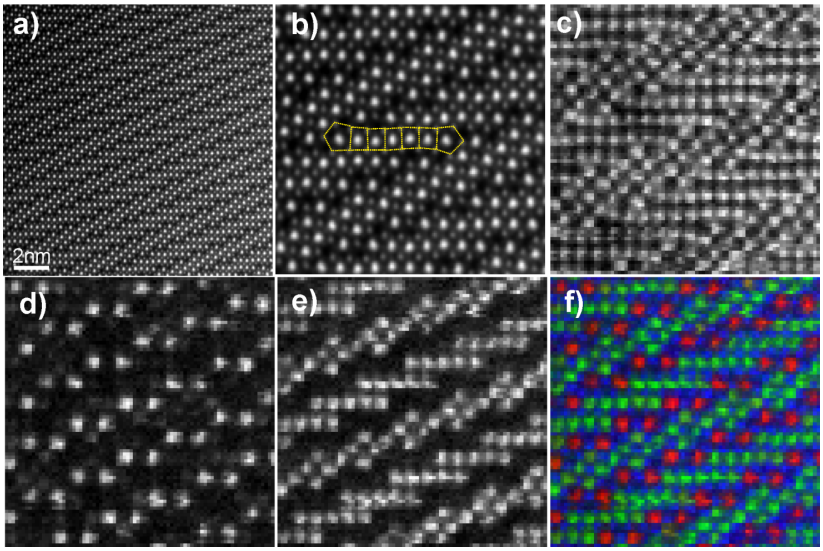

Figure 6. *[010] HAADF-EELS data for composition n=0 cooled at 1°C/hr. a) HAADF image after rigid registration of a stack of images, as described in the methods section. b) Enlarged section of the HAADF image showing the unit cell (including a slight shear due to the mis-calibrations of the scan system). c-e) Ti $L_{2,3,}$ Ba $M_{4,5}$ and Nd $M_{4,5}$ EELS maps, respectively. f) Ti, Ba and Nd RGB composite map (blue, red and green, respectively).*

Refinement of the unit cell for each composition was performed using the procedure outlined in the methods section above and overlaid positions for Ba and Nd sites in the unit cells for each sample are shown in Figure 7a. As will be clear to the reader, any differences in the determined Ba and Nd positions across the different compositions are much smaller than the uncertainties. Similar

conclusions were found for the three n=0 samples cooled at different rates, Figure 7b, although scrutinising the data, it is possible to notice a small difference in Ba positions whereas the Nd positions are unchanged as the cooling rate reduced from 60ºC/hr to 1ºC/hr. Within the precision of our experiments, it can be nevertheless concluded that the fractional coordinates for Ba and Nd columns are the same for all compositions and all cooling rates.

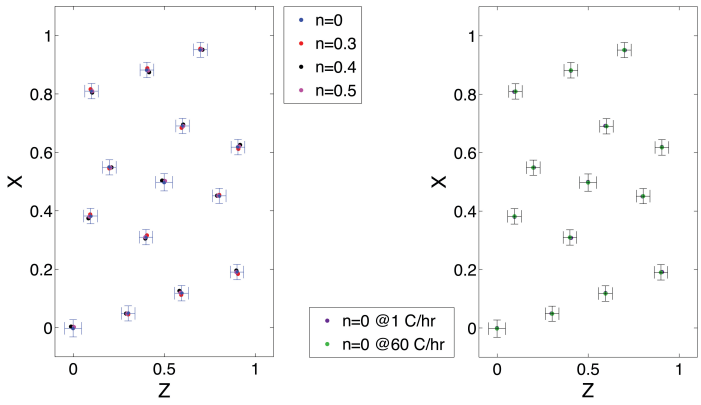

Figure 7. *Comparison of the refined average Ba and Nd positions in samples with a range of compositions from n=0 to n=0.5, error bars are 3σ for clarity; b) Comparison of average unit cells from two different n=0 samples cooled at two different rates, error bars are 3σ, as before.*

A detailed examination of the HAADF images shows an additional feature of interest, as is indicated in Figure 8. Certain columns consistently appear as non-circular and are elongated in one consistent direction. Specifically, the Ba columns and the Nd[2] columns both show significant elongation, as indicated by the arrows in Figure 8. This could indicate that these columns are not straight in this projection but involve some zigzag arrangement of atoms along the column. This, of course, is not uncommon in complex oxides as a consequence of octahedral tilting and/or antipolar ordering of A-site cations, and similar structural orderings were already foreseen in earlier Rietveld refinements from diffraction data[24-26] and are consistent with the lattice parameter doubling along the [010] direction. The tilt pattern visible in Figure 8 is closest to that of Tang *et al.*[26], but displays some slight differences, nonetheless. In the previous refinement, the off-centring of the Nd[2] position is in a direction that does not correspond to the images, although the off-centring associated with the two Ba positions appears approximately in the right direction.

Attempts were made to fit the non-round intensity peaks seen in Figure 8a with 2D elliptical functions (including degrees of freedom for elliptical peak shapes with major and minor axes, as well as with an angle-of-tilt of the major axis). Unfortunately the scatter of the best fitting parameters was rather large and there appeared to be little correlation in the tilts between nominally symmetrically-equivalents column types, indicating that the obtained results may not be fully reliable. This approach may benefit from recent progress in high-precision imaging making use of e.g. non-rigid registration[53,54]. In the present case, however, we applied for simplicity a qualitative

approach and adjusted the atomic coordinates in the structure until an overlay of the structure on the image appeared right.

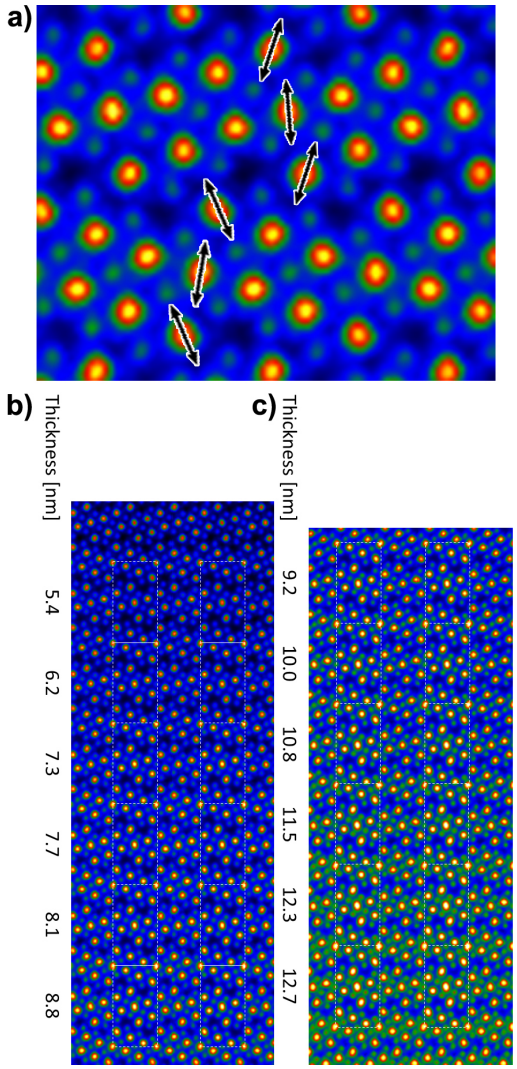

Figure 8. *Elongation of Nd[2] and Ba columns in the HAADF images (false colour, and intensity scaled, as described in the methods section) demonstrating that the columns are zigzagged in the [010] direction and matching by quantitative image simulations: a) HAADF image showing the elongation of Ba and Nd[2] columns (Ba-Nd-Ba arrowed in two orientations); b) overlay of simulations (in the dotted boxes) on a stripe of the image in the thinner region, the thickness for the match is indicated; c) overlay of simulations on a stripe of the image in a thicker part of the image. In all cases, the images have been adjusted to remove scan distortions prior to overlay of the image simulations.*

The model candidate structures obtained in this way were further tested by simulating HAADF STEM images. It is not expected that the estimation of the local object thickness is influenced by the small differences made in the tilt and zigzag structure assigned to the elongated intensity peaks, since the matching between simulations and experiment, as described in the methodological section above, was done only on the basis of the round, not elongated intensity peaks. Examples demonstrating visually the good correspondence between simulation and experiment are displayed

in Figure 8b for a selected area of smaller sample thickness and in Figure 8c for an area with larger sample thickness. The structure models leading to simulated images which agree well to the experiment were then chosen as the starting point for final Rietveld refinement of the XRD data. Full lists with atomic column positions along with uncertainties on positions are provided for the interested reader in Table 5.

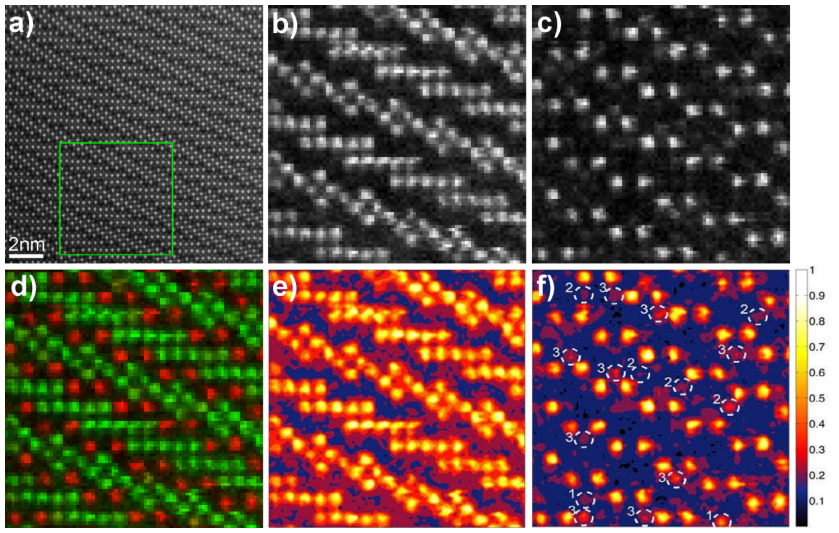

Figure 9. *a) [010] HAADF STEM survey image of the n=0 sample cooled at 1°C/hr. Atomic-resolution EELS maps of b) Nd $M_{4,5}$ and c) Ba $M_{4,5}$ and d) RGB overlay of raw Nd and Ba maps (in green and red, respectively); e) and f) normalised Nd $M_{4,5}$ and Ba $M_{4,5}$ maps, respectively, plotted after processing using the procedure for internal intensity normalization described in the methods section. Note the significant number of locations in the Barium map where significant intensity is found on Nd positions (ringed). Both b) and c) are shown on the same calibrated colour scale shown on the far right on a 0-1 scale, where 0 represents none of an element, and 1 represents the maximum intensity in the map.*

Elemental maps of Ba, Nd, Ti (and oxygen for completeness, although those are not shown here) in the [010] projection were constructed from EEL spectrum images for all samples. Representative maps for the n=0 sample slow-cooled at 1°C/hr are shown in Figure 9; in this instance each Spectrum Image was acquired using an integration time of 0.1s/pixel and a step width of ~0.08nm). The maps have been normalised into corrected areal density on each site as described in the methods section. As with the cursory intensity analysis of the HAADF images above, these maps seem to show qualitatively that the Ba is mainly concentrated on the Ba sites and the Nd sites are dominated by Nd. Similarly, Ti maps show that Ti is distributed in the expected B sites. Nevertheless, upon closer inspection, there are several Nd sites which appear to show significant concentrations of Ba on them and it can be seen that many of these sites containing noticeable Ba are columns type **3**, some are type **2** and very few (two in the example displayed in Figure 9) are type **1**. As discussed above, column types **1**, **2** and **3** are evaluated separately. For each sample, an average and standard deviation of the Ba:Nd ratio on each type of Nd column was calculated and used in the generation of the plots which summarise this analysis in Figure 10. This plot clearly

shows that little Ba is found on the Nd[1]/[5] sites, although there is a small but detectable substitution at the higher Ba contents (n=0 or n=0.3). There is more Ba on Nd[2] sites in all compositions, and this also increases at the higher Ba contents. Finally, the sites showing the highest Ba content are the Nd[3]/[4] sites, which agrees with the qualitative visual assessments of individual maps such as those shown in Figure 9.

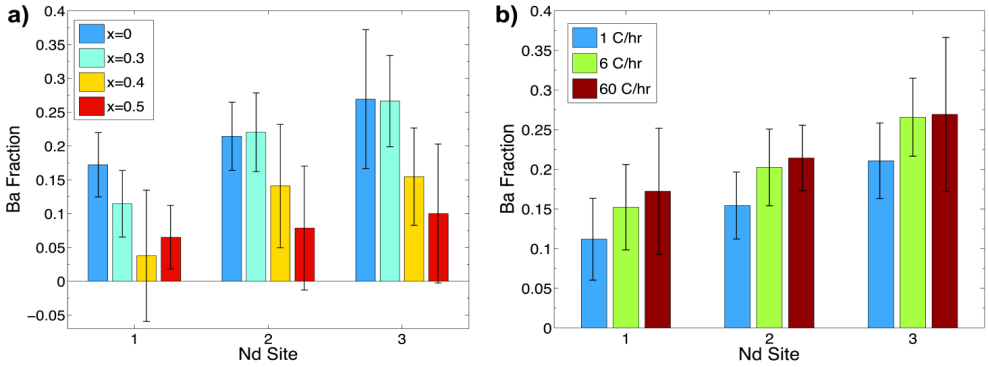

Figure 10. *Plots of the fraction of Ba on Nd columns for different samples. The error bars represent one standard deviation and represent the random variation found within the area sampled in each case: a) the dependence of Ba partitioning to the 3 column types as a function of composition, n, in the formula, $Ba_{6-3n}Nd_{8+2n}Ti_{18}O_{54}$; b) the dependence of Ba partitioning on cooling rate for the n=0 sample.*

These conclusions on the substitution behaviour of Ba onto Nd sites differ slightly from those in previous studies using X-ray diffraction.[24-26] Specifically, Tang *et al.*[26] suggest that the Nd[5] site has a high concentration of vacancies with an occupancy of just 82% following similar proposals in the earlier work of Okudera *et al.*[25] and Rawn *et al.*[24], whilst Nd[1] and other Nd sites are fully occupied. Similarly, Tang *et al.*[26] and Okudera *et al.*[25] suggested reduced occupancy on the mixed Nd[2]/Ba[3] site with a total site occupancy of about 0.9. Here, a detailed comparison of the total number of atoms on each of the different columns within each cell, as determined experimentally, found no evidence for any reduced occupancy on the Nd[2]/Ba[3] site as compared to the Ba columns or the Nd[3]/[4] columns (we note that doing the calculation on a *per cell* basis removes any effects due to thickness changes across an image). There were small hints in all four compositions that the integral intensity on the Nd[1]/[5] was slightly lower with an average occupancy of about 95%; this is discussed in more detail below. The discrepancy with earlier work may arise from the fact that no substitution of Ba onto $Nd_{3,4}$ sites was considered by Tang *et al.*[26] whereas the current work shows that these sites have consistently the highest Ba levels. Tang *et al.*[26] suggested that the Nd[2] site was 0.25 Ba:0.678 Nd in accordance with earlier suggestions from Okudera *et al.*[25]. This would be a ratio of 0.37, which is much higher than the experimentally-determined composition for the n=0 composition in the present work of about 0.2. Thus, this current work provides strong evidence that the substitution pattern of Ba onto Nd sites is significantly different to that suggested in earlier work, with significant Ba substitution onto all sites, with the

highest substitution to Nd[3]/[4] sites, some to Nd[2] sites, and the least to Nd[1]/[5] sites. This work also demonstrates the value of atomic resolution spectroscopy for understanding substitutional trends in complex mixed oxides.

We also investigated any possible relationship between cooling rate and Ba substitution onto Nd sites in the n=0 samples (*i.e.* the samples with the highest Ba content). This is summarised in Figure 10b, which indicates a weak trend towards decreased partitioning of Ba onto Nd sites for slower cooled samples. Nevertheless, the random variability from site to site is rather high as reflected in the large error bars in Figure 10b and thus this observation should be not considered as conclusive proof. If this trend were confirmed, however, it would suggest that heavy substitution of Ba onto Nd sites is energetically unfavourable, and that allowing longer times at high temperatures gives a chance for more diffusion to take place thus rearranging the structure into something more like an equilibrium structure. If so, the question arises as to where the Ba goes, since the Ba sites are all full and there is less of it appearing on all types of Nd sites. One possibility is that a small proportion of Ba diffuses to grain boundary phases: we therefore acquired a number of maps of grain boundary regions, which revealed the presence of Ba-Ti-rich phases just a few atoms thick, as shown in Figure 11. Furthermore, Ba- and Ti-rich second phases were consistently observed in the n=0 sample, as pointed out in Figure 3.

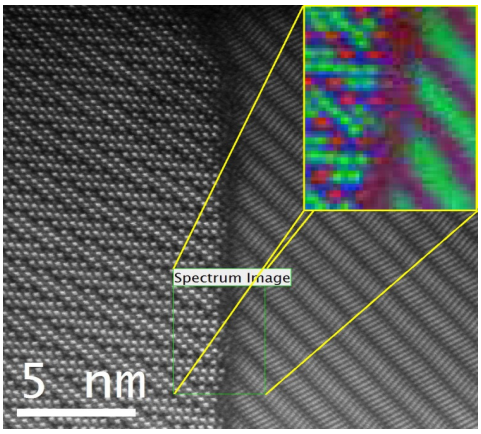

Figure 11. *A composite RGB colour map of the elemental distribution at one grain boundary in the n=0 sample cooled at 1°C/hr. Red represents Ba, green Nd, and blue Ti. Note that the boundary contains a region with no green, and is thus deficient in Nd and consequently consists of a barium titanium oxide of some form.*

We have calculated the overall content of Ba and Nd in each formula-unit for each sample of the compositional series once the experimentally-determined Ba content on the different Nd sites is taken into account and the pure Ba sites are assumed to be 100% occupied. The results of this validation are shown in Figure 12 and agree remarkably well with the $Ba_{6-3n}Nd_{8+2n}Ti_{18}O_{54}$ formula targeted in this work, giving confidence that the normalisation approach adopted is effective. This excellent agreement between the trends observed in random partitioning of individual Ba atoms

onto Nd sites and the overall targeted composition of the samples gives us a lot of confidence in the reliability and usefulness of this kind of atomic-resolution normalised analysis of compositional trends. Additionally, this provides us with strong evidence that the targeted compositions are being very accurately reproduced in most samples and moreover that the vast majority of the excess barium in each composition is partitioning effectively to neodymium sites and is not forming any significant quantity of Ba-rich second phases at grain boundaries or triple points. Thus we can have great confidence from this work that the methods employed in the production of these samples promote a high degree of homogeneity in the samples. This means that the dielectric properties that are so key to the application of these material (i.e. dielectric constant, ε_r, high Q factor, and temperature coefficients of ε_r near to zero) are all intrinsic properties of the solid solutions and not a result of any core-shell effects (such as can be the case in many dielectric capacitor materials).

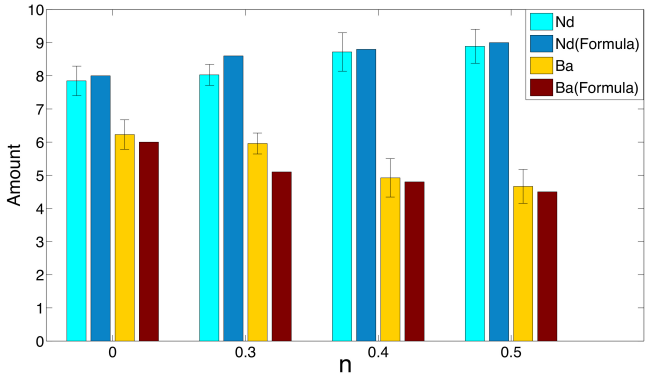

Figure 12. *Comparison of total Ba and Nd formula content as quantified from the column contents determined using EELS-SI compared with ideal values for the formula* $Ba_{6-3n}Nd_{8+2n}Ti_{18}O_{54}$. *The y axis of the plot is simply the number of atoms per formula unit.*

The vacancy distribution on Ba and Nd sites is shown in Figure 13. For the Ba, Nd[2] and Nd[3]/[4] columns, this seems to be very close to 100% suggesting that these columns are fully occupied. For the Nd[1]/[5] column this seems to be around 95%, and it is striking that this is consistent for all four samples on this plot. Whilst there is considerable variation from one unit cell to the next, as indicated by the larger uncertainty bars, it seems at least plausible that there may be a slight drop of occupancy on this column. At the very least, it appears that if there is to be a vacancy on an A site in the structure, this is the most likely location.

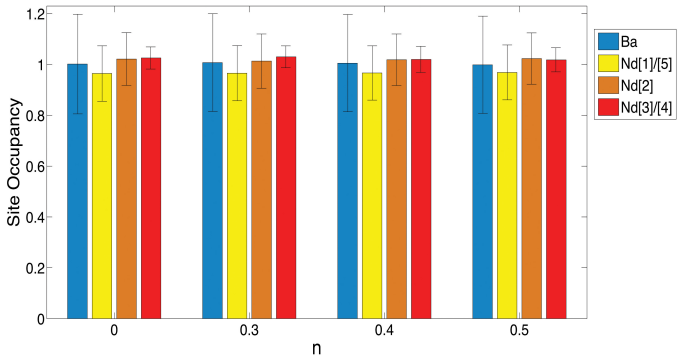

Figure 13. *Plots of total average atomic contents on each column in each sample (i.e. Ba+Nd). There seems to be a slight dip on the Nd[1]/[5] column of about 5%.*

By combining the refined atomic positions determined above in section *(2)* and the partitioning of Ba to Nd sites determined in section *(3)* we can compile an updated list of atomic coordinates for each composition. Note that the titanium and oxygen positions were not refined by us and are simply reproduced from the earlier work of Tang *et al.*[26]. The refined structures and site occupancies are summarised in Table 5 and Table 6. Electronic files of the structures in CIF format are available on request.

Table 5 *Final refined structure by combining data from this study on A-site positions and the work of Tang et al.*[26] *on O and Ti positions*

Position	x	y	z	Position	x	y	Z
Ba[1]	0.8023	0.2500	0.9110	O[9]	0.2580	0.4870	0.1710
Ba[2]	0.6855	0.2500	0.4010	O[10]	0.3290	0.7500	0.0840
Nd[1]	0.9510	0.2500	0.2990	O[11]	0.4000	0.2500	0.4010
Nd[2]	0.4940	0.2500	0.5020	O[12]	0.3470	0.2500	0.1240
Nd[3]	0.1200	0.2500	0.4040	O[13]	0.5220	0.7500	0.0220
Nd[4]	0.3810	0.2500	0.9040	O[14]	0.4570	0.2500	0.7180
Nd[5]	0.0490	0.2500	0.7010	O[15]	0.2820	0.7500	0.8440
O[1]	0.4070	0.4700	0.5580	O[16]	0.2880	0.2500	0.8010
O[2]	0.4740	0.5360	0.8520	O[17]	0.4230	0.7500	0.6730
O[3]	0.4270	0.5700	0.0570	O[18]	0.3930	0.7500	0.4310
O[4]	0.3610	0.4990	0.7640	Ti[1]	0.5000	0.5000	0.0000
O[5]	0.3170	0.4630	0.9600	Ti[2]	0.3364	0.5130	0.1150
O[6]	0.3780	0.5060	0.2490	Ti[3]	0.3909	0.5090	0.4000

O[7]	0.4780	0.5020	0.3690	Ti[4]	0.4343	0.4850	0.6990
O[8]	0.2010	0.5360	0.9160	Ti[5]	0.2608	0.4980	0.8349

Table 6. *Site occupancies for the different compositions studied in this work. (Uncertainties in brackets). Lattice parameter from Tang et al.[26] (a=22.3479Å, b=7.6955Å, c=12.2021Å).*

Site	n=0.5 60°C/hr	n=0.4 60°C/hr	n=0.3 60°C/hr	n=0 60°C/hr	n=0 6°C/hr	n=0 1°C/hr
Nd[1]: Nd	0.94(5)	0.96(10)	0.89(5)	0.83(8)	0.85(5)	0.89(5)
Nd[1]: Ba	0.06(5)	0.04(10)	0.11(5)	0.17(8)	0.15(5)	0.11(5)
Nd[2]: Nd	0.92(9)	0.86(9)	0.78(6)	0.79(4)	0.80(5)	0.85(4)
Nd[2]: Ba	0.08(9)	0.14(9)	0.22(6)	0.21(4)	0.20(5)	0.15(4)
Nd[3]: Nd	0.90(10)	0.85(7)	0.73(7)	0.73(10)	0.73(5)	0.79(5)
Nd[3]: Ba	0.10(10)	0.15(7)	0.27(7)	0.27(10)	0.27(5)	0.21(5)
Nd[4]: Nd	0.90(10)	0.85(7)	0.73(7)	0.73(10)	0.73(5)	0.79(5)
Nd[4]: Ba	0.10(10)	0.15(7)	0.27(7)	0.27(10)	0.27(5)	0.21(5)
Nd[5]: Nd	0.94(5)	0.96(10)	0.89(5)	0.83(8)	0.85(5)	0.89(5)
Nd[5]: Ba	0.06(5)	0.04(10)	0.11(5)	0.17(8)	0.15(5)	0.11(5)

(4) Computational validation

To demonstrate the preferential Ba substitution on Nd sites in the tetragonal columns follows the order column type **3** > column type **2** > column type **1**, as seen in experimental findings, we have performed DFT calculations on $Ba_{6-3n}Nd_{8+2n}Ti_{18}O_{54}$ (n=0) with selected configurations with respect to column occupancies. We found that the order of stability (from the most stable to the least stable) for Ba substitution follows $100\%COL3_{0.5}$ > $50\%COL3_1$ > $100\%COL2_1$ > $100\%COL1_{0.5}$ > $50\%COL1_1$ (0 > 10 > 16 > 27 > 50; relative energies in $kJmol^{-1}$ per $Ba_{6-3n}Nd_{8+2n}Ti_{18}O_{54}$ formula unit), in line with the experimental evidence that substitution in column type **3** is more favourable, followed by column **2** and column **1**. Focussing our attention on the 100% substitution of Ba in the different tetragonal columns, namely $50\%COL1_1$, $100\%COL2_1$ and $50\%COL3_1$, we found that substitution of Ba onto Nd sites is less favourable by 39 and 5 $kJmol^{-1}$ in column types **2** and **1**, respectively, compared to column type **3**. Thus, the order of thermodynamic stability follows $50\%COL3_1$ > $100\%COL2_1$ > $50\%COL1_1$in line with the experimental findings. However, to reduce Ba-Ba nearest-neighbour interactions inside the column and its effect on Ba substitution, we have simulated $100\%COL1_{0.5}$ and $100\%COL3_{0.5}$ where Ba substitution occurred in 100% of column types **1** and **3** respectively, but with only 50% of substitution in each column resulting in Ba ions in the columns always being surrounded by Nd ions. We found that $100\%COL1_{0.5}$ and $100\%COL3_{0.5}$

have more favourable relative energies of 23 and 10kJmol^{-1} respectively, compared to 50%COL1$_1$ and 50%COL3$_1$. This demonstrates again that no matter the arrangement of Ba, more favourable Ba substitution occurs in columns type **3** than columns type **1**, but more importantly, that Ba substitution will reduce Ba-Ba nearest-neighbour interactions. It is worth noting that our calculations only account for thermodynamic stability. Kinetic effects are not considered although they do affect the distribution of Ba in the tetragonal columns, as shown by the site occupancy in Table 4, where for composition $Ba_{6-3x}Nd_{8+2x}Ti_{18}O_{54}$ (n=0), the cooling rate changes drastically the concentration of Ba in the tetragonal columns.

V. Conclusions

We have synthesized single-phase, highly-pure and homogeneous dielectric ceramic samples of $Ba_{6-3n}Nd_{8+2n}Ti_{18}O_{54}$ (n=0-0.5) and demonstrated that their properties are intrinsic to the solid solution and not to core shell effects such as is the case of many other dielectric materials. Structural refinement was obtained from high resolution X-ray data using the Pnma space group for all compositions, which is consistent with our electron microscopy determination. Our results showed also the loss of n-glide and mirror plane symmetry compared to previous studies, which is also supported by an elongation of Nd[2] and Ba atomic columns in the pentagon sites shown by HAADF, Z-contrast and simulated images.

The paramount result is the unambiguous determination of Ba/Nd distribution within the perovskite-like tetragonal sites in the structure, which was provided at the atomistic scale. This has been achieved by the combined application of experimental and computational techniques by the analysis of EELS data, X-ray diffraction occupancy data along with DFT calculations. The current work provides evidence that the substitution pattern of Ba onto Nd sites is significantly different to that suggested in earlier work, with a clear order of preference for Ba substitution initially on Nd[3]/[4] followed by Nd[2] and Nd[1]/[5] sites. The excellent agreement between different techniques and between the trends observed in random partitioning of individual Ba atoms onto Nd sites and the overall targeted composition of the samples, showed that atomic-resolution analysis of compositional trends can be achieved reliability.

This complementary research shows that the tools described here can be used to analyze materials reliably and furthermore is not only confined to specific applications. In this case, an oxide dielectric material with a perovskite-like structure, $Ba_{6-3n}Nd_{8+2n}Ti_{18}O_{54}$, that has a distinct superstructure and defect distribution, which will be of considerable value where materials properties are largely modified by the nanostructuring; for example for thermoelectric applications where such a complex superstructure and compositional distribution is likely to have an impact on the thermal conductivity.

Acknowledgements
The authors are grateful to the EPSRC for the provision of funding for this work (EP/H043462,EP/I036230, EP/J000620, EP/K022156 acknowledged by RF) and continued funding for the SuperSTEM facility since 2002 (including EP/D040205/1, EP/D040396/1, EP/D040566/1, and the current support as an EPSRC National Facility for Aberration-Corrected Scanning Transmission Electron Microscopy; acknowledged by DMM, QMM, IM). The computational work was funded by EPSRC Programme grants EP/K016288/1 and EP/I03601X/1 (acknowledged by SCP). Computations were run on ARCHER through the Materials Chemistry Consortium funded by EPSRC grant number EP/L000202 (support for SCP). The authors thank Prof. C. Tang for organizing the collection of the high resolution X-ray data and to Dr S. Day for setting up the TOPAS files and initial refinement of the data. All computational data supporting this study are openly available from the University of Bath data archive at http://doi.org/10.15125/BATH-00174.

Supporting Information Available: An X-ray crystallographic file (CIF) and interatomic distances.

Corresponding Author
*Phone: (+44)-161-306-3564. Fax (+44)-161-275 4865. E-mail: Robert.Freer@manchester.ac.uk

References

(1) Vanderah, T. A. *Science* **2002**, *298*, 1182−1184.

(2) Reaney, I. M.; Iddles, D. *J. Am. Ceram. Soc*. **2006**, *89*, 2063−2072.

(3) Freer, R.; Azough, F. *J. Europ. Ceram. Soc*. **2008**, *28*, 1433−1441.

(4) Sebastien, M. T. *Dielectric Ceramics for Wireless Communication*; 1st ed.; Elsevier Science: Amsterdam, The Netherlands, **2008**.

(5) Cruikshank, D. B. *Microwave Materials for Wireless Applications*; Artech House: Norwood Massachuset, MA, **2011**.

(6) Ohsato, H. *J. Europ. Ceram. Soc*. **2001**, *21*, 2703−2711.

(7) Ohsato, H. *J. Ceram. Soc. Jpn.* **2005**, *113*, 703−711.

(8) Ubic, R.; Reaney, I. M.; Lee, W. E. *Int. Mater. Rev*. **1998**, *43*, 205−219.

(9) Bolton, R.L. *Temperature Compensating Ceramic Capacitors in the System Baria − Rare Earth Oxide − Titania.* PhD thesis, University of Illinois, **1968**.

(10) Kolar, D.; Stadler, Z.; Gaberscek, S.; Suvorov, D. *Ber. Dtsch. Keram. Ges*. **1978**, *55*, 346−348.

(11) Kolar, D.; Gaberscek, S.; Volavsek, B.; Parker, H. S.; Roth, R. S. *J. Solid State Chem*. **1981**, *38*, 158−164.

(12) Razgon, E. S.; Gens, A. M.; Varfolomeev, M. B.; Korovin, S. S.; Kostomarov, V. S. *Zhurnal Neorg. Khimii* **1980**, *25*, 1701−1703.

(13) Razgon, E. S.; Gens, A. M.; Varfolomeev, M. B.; Korovin, S. S.; Kostomarov, V. S. *Zhurnal Neorg. Khimii* **1980**, *25*, 2298−2300.

(14) Takahashi, J.; Ikegami, T.; Kageyama, K. *J. Am. Ceram. Soc*. **1991**, *74*, 1868−1872

(15) Takahashi, J.; Ikegami, T.; Kageyama, K. *J. Am. Ceram. Soc*. **1991**, *74*, 1873−1879.

(16) Jaakola, T.; Uusimaki, A.; Rautioaho, R.; Leppavuori, S. *J. Am. Ceram. Soc*. **1986**, *69*, C234−C235

(17) Valant, M.; Suvorov, D.; Kolar, D. *Jpn. J. Appl. Phys. Part 1* **1996**, *35*, 144−150.

(18) Suvorov, D.; Valant, M.; Kolar, D. *J. Mater. Sci*. **1997**, *32*, 6483−6488.

(19) Varfolomeev, M. B.; Mironov, A. S.; Kostomarov, V. S.; Golubtsova, L. A.; Zolotova, T. A. *Zhurnal Neorg. Khimii* **1988**, *33*, 1070−1072.

(20) Ohsato, H.; Ohhashi, T.; Nishigaki, S.; Okuda, T.; Sumiya, K.; Suzuki, S. *Jpn. J. Appl. Phys.* **1993**, *32*, 4323−4326.

(21) Matveeva, R. G.; Varfolomeev, M. B.; Ilyushchenko, L. S. *Zhurnal Neorg. Khimii* **1984**, *29*, 31−34.

(22) Azough, F.; Champness, P. E.; Freer, R. *J Appl Crystallogr* **1995**, *28*, 577−581.

(23) Rawn, C. J. In *Electroceramics V*; Baptista, J. L., Labrincha, J. A., Vilarinho, P. M., Eds.; Proceedings of the International Conference on Electronic Ceramics and Applications; European Ceramic Society: Aveiro, Portugal, **1996**, Book 2, pp 67-73.

(24) Rawn, C. J.; Birnie, D. P.; Bruck, M. A.; Enemark, J. H.; Roth, R. S. *J. Mater. Res*. **1998**, *13*, 187−196.

(25) Okudera, H.; Nakamura, H.; Toraya, H.; Ohsato, H. *J. Solid State Chem*. **1999**, *142*, 336−343.

(26) Tang, C. C.; Roberts, M. A.; Azough, F.; Leach, C.; Freer, R. *J. Mater. Res*. 2002, *17*, 675−682.

(27) Hofer, F. *Microsc. Microanal. Microstruct.* **1991**, *2*, 215−230.

(28) Wang, P.; D'Alfonso, A. J.; Findlay, S. D.; Allen, L. J.; Bleloch, A. L. *Phys. Rev. Lett*. **2008**, *101*, 236102(1−4).
(29) Kothleitner, G.; Neish, M. J.; Lugg, N. R.; Findlay, S. D.; Grogger, W.; Hofer, F.; Allen, L. J. *Phys. Rev. Lett.* **2014**, *112*, 085501(1−5).
(30) Xin, H. L. L.; Dwyer, C.; Muller, D. A. *Ultramicroscopy* **2014**, *139*, 38−46.
(31) Warusawithana, M. P.; Richter, C.; Mundy, J. A.; Roy, P.; Ludwig, J.; Paetel, S.; Heeg, T.; Pawlicki, A. A.; Kourkoutis, L. F.; Zheng, M.; Lee, M.; Mulcahy, B.; Zander, W.; Zhu, Y.; Schubert, J.; Eckstein, J. N.; Muller, D. A.; Hellberg, C. S.; Mannhart, J.; Schlom, D. G. *Nat. Commun*. **2013**, *4*, 2351(1−9).
(32) Kimoto, K.; Asaka, T.; Yu, X.; Nagai, T.; Matsui, Y.; Ishizuka, K. *Ultramicroscopy*, **2010**, *110*, 778−782.
(33) MacLaren, I.; Villaurrutia, R.; Schaffer, B.; Houben, L.; Pelaiz−Barranco, A. *Adv. Func. Mater*. **2012**, *22*, 261−266.
(34) MacLaren, I.; Wang, L. Q.; Schaffer, B.; Ramasse, Q. M.; Craven, A. J.; Selbach, S. M.; Spaldin, N. A.; Miao, S.; Kalantari, K.; Reaney, I. M. *Adv. Func. Mater*. **2013**, *23*, 683−689.
(35) MacLaren, I.; Wang, L. Q.; Morris, O.; Craven, A. J.; Stamps, R. L.; Schaffer, B.; Ramasse, Q. M.; Miao, S.; Kalantari, K.; Sterianou, I.; Reaney, I. M. *APL Materials* **2013**, *1*, 021102(1−7).
(36) Houben, L. (2009). *iMtools Software Package for Digital Image Processing of Electron Micrographs, Research Center Jülich.* Available at http://www.er−c.org/methods/software.htm, Accessed September 8, **2015**.
(37) Houben, L.; Thust, A.; Urban, K. *Ultramicroscopy* **2006**, *106*, 200−214.
(38) Dwyer, C.; Maunders, C.; Zheng, C. L.; Weyland, M.; Tiemeijer, P.C.; Etheridge, J., *Appl. Phys. Lett*. **2012**, *100*, 191915(1−4).
(39) LeBeau, J.M.; Findlay, S. D.; Allen, L. J.; Stemmer, S., *Phys. Rev. Lett*. **2008**, *100*, 206101(1−4).
(40) Kresse, G.; Hafner, J. *Phys. Rev. B* **1994**, *49*, 14251−14269.
(41) Kresse, G.; Furthmuller, J. *Phys. Rev. B* **1996**, *54*, 11169−11186.
(42) Blochl, P. E. *Phys. Rev. B* 1994, *50*, 17953−17979.
(43) Kresse, G.; Joubert, D. *Phys. Rev. B* **1999**, *59*, 1758−1775.
(44) Dudarev, S. L.; Botton, G. A.; Savrasov, S. Y.; Humphreys, C. J.; Sutton, A. P. *Phys. Rev. B* **1998**, *57*, 1505−1509.
(45) Anisimov, V. I.; Zaanen, J.; Andersen, O. K. *Phys. Rev. B* **1991**, *44*, 943−954.
(46) Morgan, B. J.; Watson, G. W. *J. Phys. Chem. C* **2010**, *114*, 2321−2328.
(47) Molinari, M.; Tompsett, D. M.; Parker, S. C.; Azough, F.; Freer, R. *J. Mater. Chem. A* **2014**, *2*, 14109−14117.
(48) Molinari, M.; Parker, S. C.; Sayle, D. C.; Islam, M. S. *J. Phys. Chem. C* **2012**, *116*, 7073–7082.
(49) Watson, G.W.; Kelsey, E.T.; de Leeuw, N.H.; Harris, D.J.; Parker, S.C. *J. Chem. Soc.,* Faraday Trans. **1996**, *92*, 433−438.
(50) Momma, K.; Izumi, F., *J. Appl. Crystallogr*. **2008**, *41*, 653−658.
(51) Zheng, C.; West, A.R. *Brit. Ceram. Proc*. **1992**, *49*, 247−250.
(52) Stephens, P.W. *J. Appl. Cryst*. **1999**, *32*, 281-289.
(53) Jones, L.; Yang, H.; Pennycook, T.J.; Marshall, M.S.J.; Van Aert, S.; Browning, N.D.; Castell, M.R; Nellist, P.D. *Adv. Struct. Chem. Imag*. **2015**, *1*:8, 1−16
(54) Sang, X.H.; LeBeau, J.M. *Ultramicroscopy* **2014**, *138*, 28−35.

For Table of Contents Only

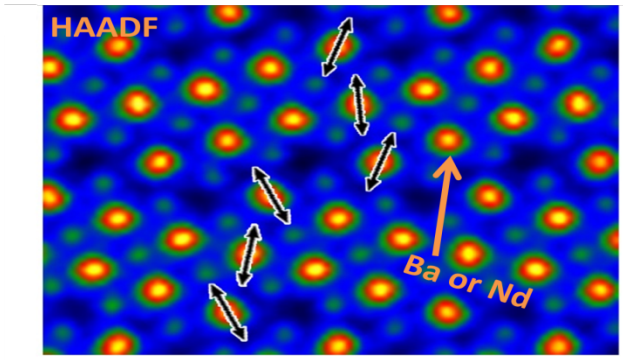

The defect distribution in complex superstructured $Ba_{6-3n}Nd_{8+2n}Ti_{18}O_{54}$ was evaluated using Synchrotron X-ray, EELS and DFT. This will affect properties of microwave dielectric and thermoelectric ceramics.